Recombination effects in laser-driven acceleration of heavy ions

S. Morris and D. O. Gericke
Centre for Fusion, Space and Astrophysics, Department of Physics, University of Warwick, Coventry CV4 7AL, United Kingdom

S. Fritzsche
Helmholtz-Institut Jena, Fröbelstieg 3, 07743 Jena, Germany;
Theoretisch-Physikalisches Institut, Friedrich-Schiller-Universität Jena, 07743 Jena, Germany;
and GSI Helmholtzzentrum für Schwerionenforschung, 64291 Darmstadt, Germany

J. Machado and J. P. Santos
LIBPhys-UNL, Departamento de Física, Faculdade de Ciências e Tecnologia, NOVA FCT, Universidade Nova de Lisboa, 2829-516 Caparica, Portugal

M. Afshari
Center for Advanced Systems Understanding CASUS, 02826 Görlitz, Germany
and Helmholtz-Zentrum Dresden-Rossendorf, Bautzner Landstraße 400, 01328 Dresden, Germany

(Received 6 November 2024; accepted 30 April 2025; published 16 June 2025)

Recombination effects are shown to modify the charge-state distribution achieved in the acceleration of heavy ions during high-intensity laser-solid interactions. A recombination package has been developed for particle-in-cell codes, which includes dielectronic, radiative, and three-body recombination. One-dimensional simulations were then performed to model a recent experiment, where 4.1×10^{20} W cm^{-2} laser pulses heated thin gold targets to produce gold ion beams. Simulations show that the ion beams from 100-nm targets were unaffected by recombination, but that recombination caused charge states to drop in 300-nm targets, similar to experimental observations. These differences were attributed to target temperature, as 300-nm targets were heated to lower temperatures than 100-nm targets during the laser-target interaction, causing ions to spend more time in environments where recombination rates dominated ionization rates.

DOI: 10.1103/PhysRevE.111.065209

I. INTRODUCTION

Laser-driven acceleration of heavy ions is an area of high interest, renewed by recent experiments which successfully accelerated ions to kinetic energies exceeding 1 MeV/u [1–4]. Such beams could create neutron-rich nuclei through fission-fusion reactions [5] to study the astrophysical *r* process [6]. The energy-deposition properties of these beams could also be used to heat secondary targets [7,8], create warm dense matter [9], trigger inertial fusion reactions [10,11], or to destroy cancerous tumors [12,13]. While many properties of these ion beams have already been described through simulations [14–16], some experimental results are yet to be explained.

In a recent experiment at the PHELIX laser facility, laser pulses of 500-fs duration and 4.1×10^{20} W cm^{-2} peak cycle-averaged intensity were directed at gold foils ranging from 25 to 500 nm thickness, yielding gold ions with kinetic energies exceeding 1.379 GeV (7 MeV/u) [1]. Ion charge states were found to increase with target thickness from 25 to 100 nm, with some ions reaching over Au^{70+} for the 100-nm target. This behavior was modeled by Afshari *et al.* [14] using the two-dimensional (2D) version of the EPOCH particle-in-cell (PIC) code [17], where these high charge-states could be successfully reproduced when both field ionization (FI) [18] and electron-impact collisional ionization (CI) [19] were considered. However, ion charge-states from the PHELIX experiment started to decrease as targets became thicker than 100 nm, which simulations failed to predict, modeling no change in charge-states for these thicker targets.

One of the proposed reasons for the discrepancy between experiment and simulation was the lack of recombination in EPOCH [14]. This current work seeks to determine whether recombination processes are sufficient to affect the gold ion beam in targets over 100 nm. A recombination package has been created for particle-in-cell codes and was implemented in EPOCH. The algorithm is similar to the recombination methods proposed by Wu *et al.* [20] and Khalilzadeh *et al.* [21], and includes dielectronic (DR) [22], radiative (RR) [23], and three-body (3BR) [24] recombination channels.

One-dimensional (1D) simulations have been performed for 100-nm and 300-nm gold targets, with and without recombination, and the charge states obtained from these

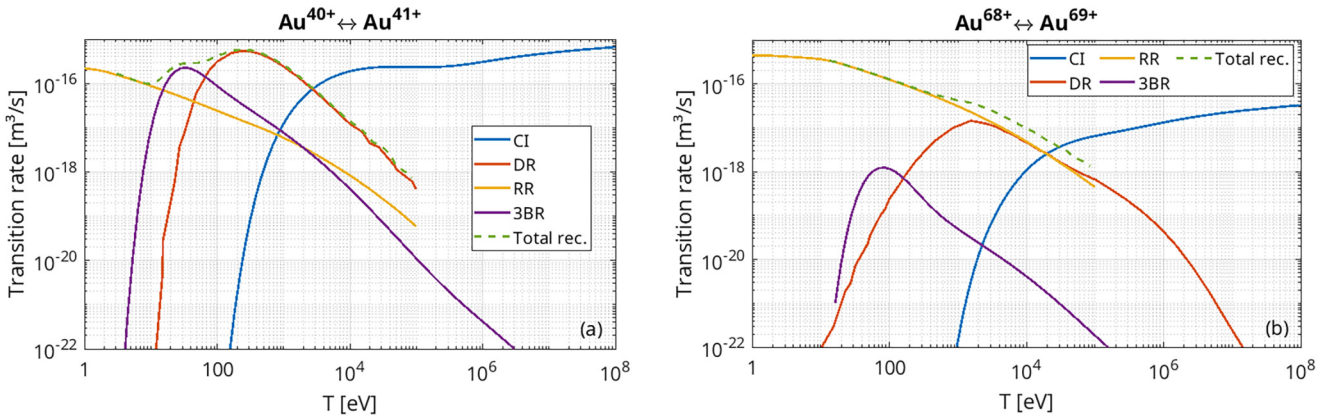

FIG. 1. Comparison of transition rates for ionization and recombination between gold ion pairs: (a) Au^{40+} and Au^{41+}, (b) Au^{68+} and Au^{69+}. Rates are provided for collisional ionization (CI), the dielectronic (DR), radiative (RR), and three-body (3BR) recombination channels, and the total recombination rate for temperatures where all three are known. The 3BR rates assume a background electron number density is present which neutralizes Au^{41+} and Au^{69+} targets at solid ion-density (5.9×10^{28} m^{-3}) in (a) and (b), respectively.

simulations have been compared. Section II describes the ionization and recombination models used, and Sec. III describes the EPOCH implementation and simulation setup. The results are given in Sec. IV, which shows the effects of recombination on the target plasma and accelerated ion beam.

II. TRANSITION RATES

In this study, ionization rates between gold ions were modeled for the FI and CI processes, while recombination was modeled with DR, RR, and 3BR. For the FI model considered, rates scaled with the magnitude of the background laser fields at the ion position, and Afshari *et al.* [14] showed that these rates were important for early ionization to charge states between Au^{40+} and Au^{50+} in the PHELIX setup. The higher charge states observed in experiment could only be reproduced when the CI process was switched on. The CI, DR, RR, and 3BR processes have rates, α, which scale with the background electron temperature, and these rates are shown in Fig. 1 for transitions between two pairs of high charge-state Au ions.

Figure 1 suggests that in the highly charged ions where CI is important, ionization does not dominate recombination until electron temperatures reach the order of 1–10 keV, with higher charge-states requiring greater temperature. 3BR is seen to be negligible even at high electron densities, with DR and RR providing the dominant channels for recombination.

The rates quoted in Fig. 1 refer to

$$\alpha = \langle \sigma(E_k) v_e(E_k) \rangle_e, \tag{1}$$

where σ is the transition cross-section for a given process, and v_e is the speed of the incident electron triggering ionization for CI, or being captured for recombination. Both terms are functions of the incident electron kinetic energy E_k, and the average $\langle ... \rangle_e$ is performed over the distribution of local electrons. Here it is assumed that electrons follow a Maxwell-Jüttner (MJ) distribution of E_k values for a given temperature, switching to Maxwell-Boltzmann when the MJ exponential term exceeds machine precision.

Over a small time interval dt, the probability $P(dt)$ of a single incident electron triggering CI, or being captured in recombination, is

$$P(dt) = \sigma v_e n_i dt, \tag{2}$$

using the cross section for the corresponding transition σ, where n_i is the local ion number density. Hence, $\alpha n_i dt$ gives the probability that a typical electron triggers an ion transition over time dt. A longer period Δt may be broken into successive small chances, $ndt = \Delta t$, such that the probability of no transition over the interval, $P_{\text{no}}(\Delta t)$, is

$$P_{\text{no}}(\Delta t) = \left[1 - \left(\sigma v_e n_i \frac{\Delta t}{n}\right)\right]^n, \tag{3}$$

and in the limit of $n \to \infty$, $dt \to 0$, and the probability of at least one transition becomes

$$P(\Delta t) = 1 - \exp(-\alpha n_i \Delta t). \tag{4}$$

As the incident electron is captured in recombination, only one transition is possible, and Eq. (4) describes the probability of recombination during Δt. However, an incident electron can perform collision ionization with multiple ions over Δt, and Eq. (4) does not describe the number of ionization transitions during this interval.

In this work, the simulation time step, Δt, is set to be sufficiently small such that the probability of more than one transition over Δt is negligible, and Eq. (4) is treated as the transition probability. The following sections discuss the details of the rate calculations used for the transition α.

A. Ionization

FI refers to ionization produced when bound electrons are exposed to strong external electromagnetic fields. The laser is assumed to provide the dominant source of FI in these interactions, so direct-photon ionization has been neglected, as lasers like PHELIX have photon energies much lower than gold binding energies. Instead, the FI model of EPOCH was used [25], which combines multiphoton ionization [26], tunneling ionization [27], and a classical extrapolation for over-the-barrier ionization [28].

CI considers the ionization caused when incident free electrons collide with bound electrons, transferring sufficient

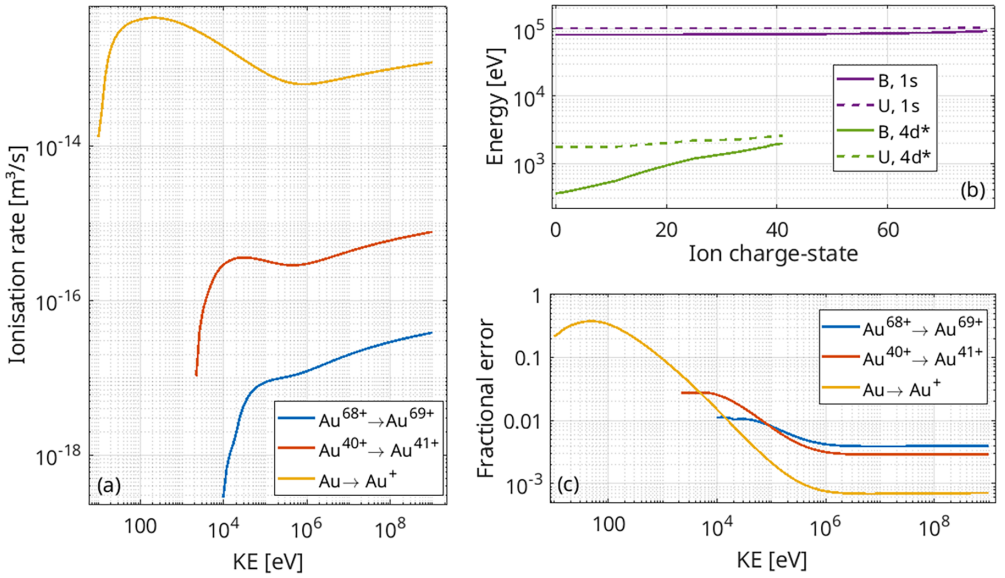

FIG. 2. Effects of the $B = U$ approximation in the RBEB collisional ionization model, for various gold ions. The RBEB rates are shown in (a) without the $B = U$ approximation, values of B and U for different shells are given in (b), and (c) gives the fractional change in the (a) rates when the $B = U$ approximation is used. In panel (b), $4d^*$ describes a shell with total angular momentum $J = |L + S| = 3/2$, where L and S denote the orbital and spin angular momenta, respectively.

energy to let both electrons escape the ion. The CI rates were given by the relativistic binary-encounter-Bethe (RBEB) model [19,29]. These rates rely on the binding energies of each electron shell, B, and also the mean kinetic energy of bound electrons, U. Due to a lack of readily available data for U, PIC codes tend to use a $B = U$ approximation [19], but it has been suggested that this may contribute to the experiment-simulation disagreement under investigation in this paper [14]. Hence, to test their significance, U values have been calculated specifically for this work.

B and U values were obtained from first principles by calculating the single-configuration Dirac-Fock wave functions of each gold ion. These calculations were carried out using the *ab initio* `mdfgme` code [30,31], which applied the multiconfiguration Dirac-Fock (MCDF) method. The Breit interaction was fully accounted for, and nuclear size effects were incorporated through a Fermi model, utilizing atomic masses and mean spherical radii from the tables of Audi *et al.* [32] and Angeli [33], respectively. The calculations focused on ground-state ions, with electron configurations taken from the tables of Rodrigues *et al.* [34].

Figure 2 shows tests of the $B = U$ approximation. Values of B and U are compared for some shells, which shows the two terms typically vary together within a factor of 10. The resultant CI rates are shown using the separate B and U values, and the fractional error introduced when switching to $B = U$ is also given. While the deviation is over 10% for ions at low temperature and charge state, the high-temperature high-charge rates show little difference. Despite the change in rates being small, the CI model used in this paper will still use the B and U energies obtained from `mdfgme`.

B. Recombination

The RR and DR rates used in this paper have mostly been taken from the tabulated rates given by the `FLYCHK` code [35]. In RR, electrons recombine with ions while emitting the excess energy as radiation, and `FLYCHK` calculates RR rates using detailed balance. Here, the Kramers photoionization cross-section is used to get ionization rates [23], and the inverse recombination rates are taken from the Saha-Boltzmann equation.

In DR, recombination proceeds via a two-step process. An incident electron is first captured to form a doubly excited ion, which then relaxes through photon emission [36]. In addition to the tabulated `FLYCHK` data, DR rates were also calculated for recombination from Au^{68+} and Au^{69+} using the Jena Atomic Calculator (`JAC`) toolbox [36,37]. `JAC` obtained DR rate coefficients using a cascade-type computation in which the relevant configurations in the formation of the doubly excited resonances were treated independently and were generated automatically [38]. This approach models electron capture into an $n\ell$ shell, followed by a step-wise decay to the ion ground-state. Various empirical rules were used to estimate, for instance, the allowed core excitations or the shells of the captured electron. Resonances have been included up to 2×10^3 Hartree above the initial ground level, as well as single excitations of the $3s$ and $2p$ core electrons for (initially) Au^{68+} and Au^{69+} ions, respectively. Capture into shells with $n \leqslant 10$, $\ell \leqslant 5$ was allowed, as well as excitations of the core shell electron into the $n\ell \leqslant 4f$ shells.

Figure 3 compares the DR plasma rates from `FLYCHK` with computations by `JAC` for initial charge-states Au^{68+} and Au^{69+}. Deviations occur especially at low plasma temperatures, where the rate coefficients are known to be sensitive to the low-lying resonances. These resonances close to the autoionization threshold are not well represented in both codes, neither for their correct position nor the resonance strength. However, such disagreements will have little relevance for the high temperatures achieved in our system of interest. The DR model implemented in this paper uses the `JAC` rates calculated

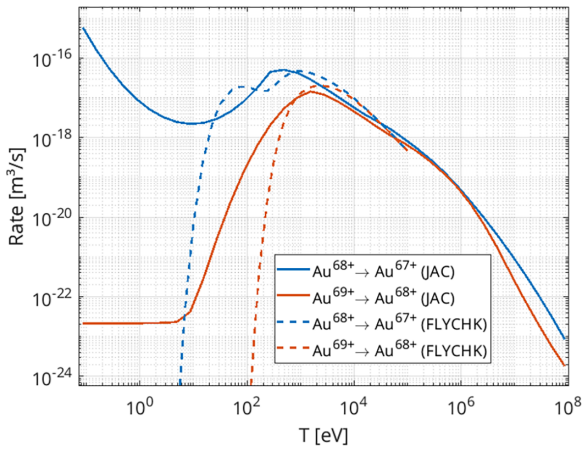

FIG. 3. A comparison of DR rates evaluated using the FLYCHK and JAC codes.

for the two transitions shown in Fig. 3, as FLYCHK rates are only tabulated to 100 keV. The model switches to FLYCHK rates otherwise.

Finally, 3BR refers to the inverse process of CI. Here, two electrons collide in the field of an ion, and one loses enough energy in the collision to prevent it from escaping the ion fields. Tabulated 3BR rates are not available from FLYCHK, so a model has been used which is mainly based on detailed balance [24]. The rate of change of electron number density n_e due to the 3BR process is given by

$$\frac{dn_e}{dt} = \sum_Q \sum_j \left(-n_e n_{i,Q+1} \alpha^{\mathrm{3BR}}_{j,Q}\right), \tag{5}$$

where the sum is performed over all ion charge-states Q and bound electron shells j. Here, $n_{i,Q+1}$ is the number density of ions with charge-state $Q+1$, and $\alpha^{\mathrm{3BR}}_{j,Q}$ is the 3BR rate from $(Q+1)$ to Q, where a new bound electron is added to shell j. The rate term for nondegenerate plasma is given by

$$\alpha^{\mathrm{3BR}}_{j,Q} = g_{j,Q} n_e \left(\frac{2\pi\hbar^2}{m_e k_B T_e}\right)^{3/2} \alpha^{\mathrm{CI}}_{j,Q} \exp\left(\frac{I_{j,Q}}{k_B T_e}\right), \tag{6}$$

where $g_{j,Q}$ and $I_{j,Q}$ are the statistical weight and ionization energy for electrons in ion Q shell j, respectively, and $\alpha^{\mathrm{CI}}_{j,Q}$ is the CI rate for such bound electrons [24]. Additionally, T_e is the electron temperature, and k_B, m_e, and $\hbar$ are the Boltzmann constant, electron mass, and reduced Planck constant, respectively.

While $\alpha^{\mathrm{3BR}}_{j,Q}$ is given in Eq. (6), two approximations can be made to simplify its form for our system of interest. Firstly, PIC codes model weakly coupled plasma, which carries the implicit assumption that the ionization energy is not modified. Secondly, let us assume that free electrons are always captured to the ion ground state. By comparing the ground-state configurations of ions with charge-states $(Q+1)$ and Q, the shell which gains the new electron can be identified, and only this shell is considered for j. This also allows for the use of the known ionization energy I_Q for the $Q \to (Q+1)$ transition. Hence,

$$\alpha^{\mathrm{3BR}}_{j,Q} = 2(2\ell+1) n_e \left(\frac{2\pi\hbar^2}{m_e k_B T}\right)^{3/2} \alpha^{\mathrm{CI}}_{j,Q} \exp\left(\frac{I_Q}{k_B T}\right), \tag{7}$$

where g_j has been written as $2(2\ell+1)$, the degeneracy of the shell which captures the free electron.

III. SIMULATION

The rates described in Sec. II have been implemented in the EPOCH [17] PIC code. The CI subroutine has been upgraded to remove the $B = U$ approximation, and a recombination package has been added to the code for DR, RR, and 3BR. Macroparticle weights in the recombination routines have been handled in a similar way to those for the CI method [19] and are discussed in Sec. III A. The new code was used to model the 100-nm and 300-nm target shots from the PHELIX laser to investigate the importance of recombination effects. Details on the numerical parameters used for these 1D EPOCH simulations are provided in Sec. III B.

A. Recombination model

PIC codes deal with macroelectrons and macroions instead of individual particles. These macroparticles are computational objects which represent a large number of real particles, described by the macroparticle weight. For a single electron within a macroelectron of weight W_e, the probability of recombination over a time Δt is given by Eq. (4). If each real electron within the macroelectron shares this probability of recombination, then we expect the macroelectron as a whole to create N_r recombined real ions,

$$N_r = W_e[1 - \exp\left(-\alpha(T_e) n_i \Delta t\right)], \tag{8}$$

where recombination rates are a function of the cell electron temperature, T_e. These recombination rates are only valid in the ion rest frame, where the temperature is transformed to T_e',

$$T_e' = \frac{1}{3 m_e k_B}\left(\left(\frac{1}{3}\gamma_i^2 + \frac{2}{3} + \gamma_i^2\beta_i^2\right)\langle p^2\rangle_e + (\gamma_i\beta_i m_e c)^2 - \frac{2\beta_i\gamma_i^2}{c}\langle p_x E_e\rangle_e\right), \tag{9}$$

following the procedure in Appendix A.

The recombination algorithm considers one charge-state transition at a time and acts to ensure the number of recombined macroparticles in each cell tends towards the correct number on average, by applying (8) to all macroelectrons present. Firstly, each macroelectron is randomly paired to a macroion, and T_e' is deduced. This allows N_r to be calculated for each macroelectron in the cell, sampling a range of relative velocities with cell macroions.

If N_r is less than the ion weight W_i, the macroion drops one charge-state with a probability of N_r/W_i, which yields the correct number of recombination events on average. Otherwise, the macroion is always recombined, and the fraction of recombination events the macroelectron is yet to make is

saved to the f_e variable,

$$f_e \to \left(1 - \frac{W_i}{f_e N_r}\right) f_e, \tag{10}$$

where f_e has an initial value of 1 for each macroelectron. The macroelectron is then paired to a new macroion and the process repeats, but this time the macroelectron aims for $f_e N_r$ recombined ions. This procedure continues, with f_e updating each time to track the fraction of recombined ions left to create, until $f_e N_r < W_i$, or until all macroions have recombined. After recombination, the real-particle electron momentum is added to the real-particle ion momentum for momentum conservation.

Since macroparticle weights may be different for electrons and ions, the recombination behavior for macroelectrons is modeled separately, similar to the method in Morris *et al.* [19] for CI. Macroelectrons are removed from the simulation with probability N_r/W_e, which removes the correct number of electrons on average. Two example cases have been provided in Appendix B to show how this method works in practice.

As macroelectrons are not always removed when momentum is added to macroions, individual recombination events may not conserve momentum. However, since the number of real electrons removed matches the number of real ions recombined when averaged over many particles, the total removed electron momentum will match the total momentum gained by ions on average.

While some recombination channels involve photon emission, recombination photons are not added to the simulation in this model. An implied radiation background is used for radiative recombination, and rates are sampled using the local plasma temperature. Direct photoionization is assumed to be negligible, as the simulations of Afshari *et al.* [14] demonstrate that experimental chargestates may be achieved using only field and collisional ionization.

Simple benchmarking simulations were performed to ensure the sampling behavior was independent of macroparticle weight, which are shown in Fig. 4. These simulations tracked recombination between Au^{69+} and an electron population with twice the initial ion density. One simulation considered equal macroparticle weights $W_e = W_i$ and the other used $W_e = 2W_i$. The electron temperature was set to 1 keV, and the EPOCH rates have been compared to those expected from Eq. (8). Figure 4 shows good agreement between the simulated and expected growth of the Au^{68+} species, for both weighting configurations.

B. Setup

Four 1D EPOCH simulations were performed to determine the role of recombination in a configuration similar to the PHELIX experiment. The simulation domain in all four simulations spanned from -10 to $+20$ μm in x, with a cell size of 5 nm. Neutral Au macroparticles were positioned from $x = 0$, up to either 100 nm or 300 nm depending on the simulation, and 800 macroparticles were loaded per target cell. The gold targets were initialized at rest, with a number density of 5.9×10^{28} m^{-3}. The simulations were each run to 2 ps and employed current smoothing and B-spline macroparticle shapes to suppress self-heating.

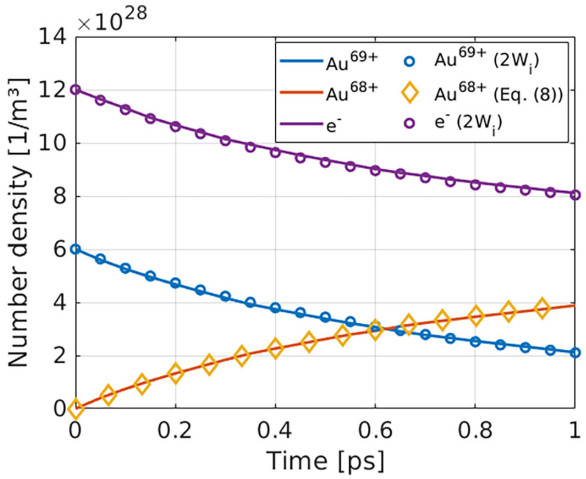

FIG. 4. EPOCH macroparticle weight benchmark, where $\alpha^{DR} = 1.1 \times 10^{-17}$ m^3/s, RR and 3BR were switched off, and only $Au^{69+} \to Au^{68+}$ was considered. Solid lines describe a simulation where $W_e = W_i$, and circles come from one with $W_e = 2W_i$. The expected growth of Au^{68+} from Eq. (8) is shown by the diamonds.

A laser pulse with a 4.1×10^{20} W cm^{-2} peak cycle-averaged intensity was injected through the $x = -10$ μm boundary. The pulse used a Gaussian temporal profile for the cycle-averaged intensity, with a 500 fs FWHM, and an initial intensity of 4.1×10^{19} W cm^{-2} on the boundary. The laser wavelength was set to 1.053 μm.

Two simulations were performed for each target thickness, with the recombination package switched on and off. All simulations included FI, CI, and elastic scatter between electrons and other electrons or ions. EPOCH uses a Nanbu-Perez scheme [39,40] for cumulative scatter collisions, and these simulations assumed a constant Coulomb logarithm, $\ln \Lambda = 5$.

The elastic scatter collisions, CI, and recombination processes were supercycled for computational speed, such that they were performed once every ten simulation timesteps, dt, for an interaction time of $10dt$. The CI process requires a small interaction time to use the probability in Eq. (4), as this makes multiple-ionization events unlikely. Assuming a peak $\alpha = 10^{-15}$ m^3/s for transitions of interest (see Fig. 1), using Poisson statistics with $10dt \approx 0.17$ fs yields a multiple-ionization probability of 5×10^{-5}, which may be treated as negligible.

Switching on this recombination algorithm doubled the 300-nm simulation run time from 3 to 6 h on 48 cores. The computational costs in 2D and 3D may be roughly estimated by multiplying these times by the number of cells in the new dimensions. For example, the domain could span 10 μm in y to model a laser with a 5-μm focal spot, meaning the number of cells and the run-time would increase by a factor of around 2000. While advantageous, higher dimensions are not required to demonstrate the effect of recombination in this work.

IV. RESULTS

The charge-state distributions in each simulation have been plotted as a function of time in Fig. 5. This figure averages

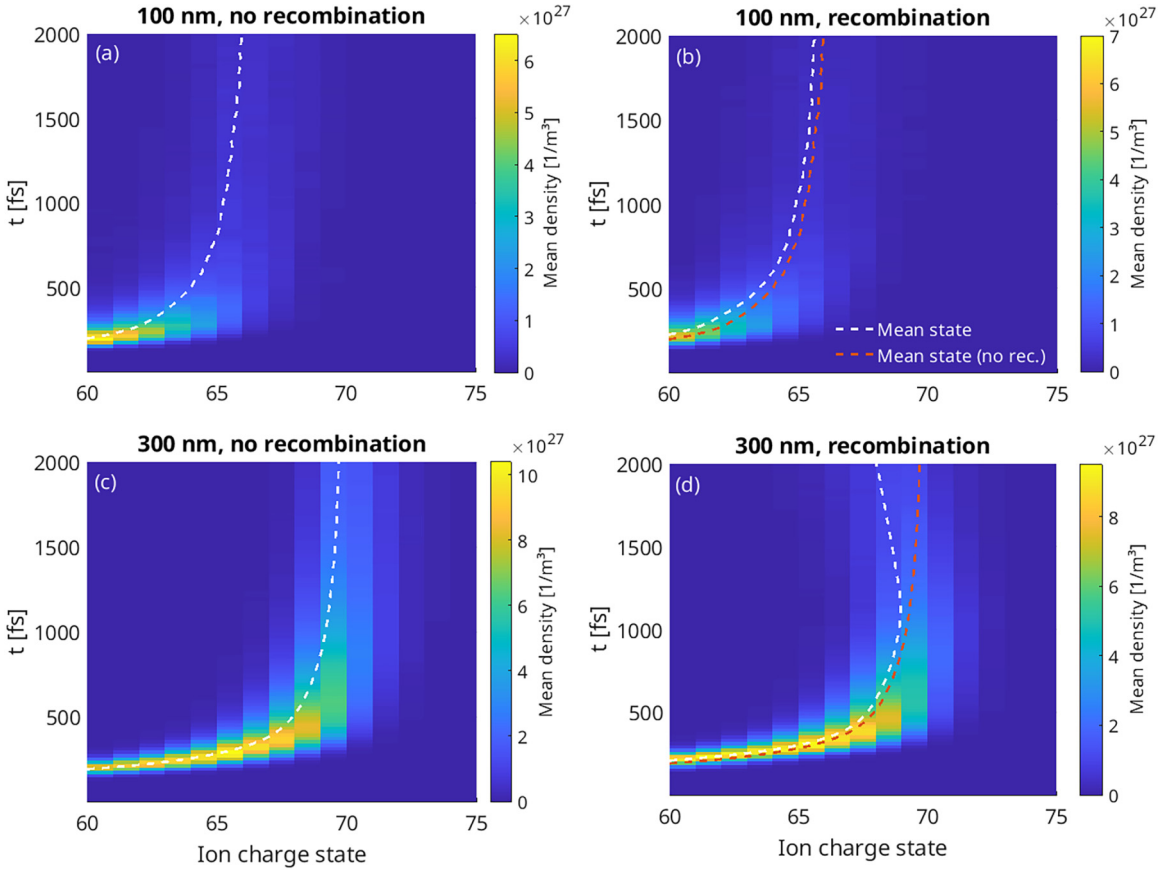

FIG. 5. Average number densities of gold ion charge-states in the initial target volume as a function of time, from different simulations. Plots (a)–(d) are labeled to show whether they describe 100-nm or 300-nm targets, in simulations with or without the recombination package switched on. The white dashed line denotes the average charge-state at each time, and the lines from (a) and (c) have been included as orange dashed lines in (b) and (d), respectively, for comparison.

the ion number densities over the region initially occupied by the target $x = 0$–100 nm for 100-nm targets, or to 300 nm for 300-nm targets. The reduction in total summed density as time progresses is therefore a result of target expansion over the 2-ps simulation time. Little difference can be seen between simulations with and without recombination for the 100-nm target, but there is a clear reduction in the highest charge-states when recombination is switched on for 300 nm. This trend is consistent with previous analysis, as the simulations performed by Afshari *et al.* [14] suggest that ionization alone is sufficient to reproduce the 100-nm charge states, while we expect no-recombination simulations to overestimate the charge states for 300-nm targets.

These trends are clearer when considering the charge-state distribution over a greater region at the end of the simulation, as shown in Fig. 6. Here, the total number of real ions with final position between $x = \pm 9$ μm have been summed for each ion species and divided by the window volume. The average charge-states in 100-nm targets are seen to drop by 0.3 from 66.0 to 65.7 when recombination is switched on, compared to a drop of 1.7 from 69.7 to 68.0 in 300-nm targets.

The change in recombination behavior from 100-nm to 300-nm targets can be explained by the evolution of simulation parameters shown in Fig. 7. Both targets can be seen to quickly heat to temperatures exceeding 100 keV, or over 1 MeV in the target region for the 100-nm case. This temperature discrepancy comes from the fixed laser energy, as a 300-nm target has more particles to share the absorbed laser energy with when compared to a 100-nm target. Temperatures in the initial target volume are significant, as this is where most of the particles are. In the limit of small Δt, the number of charge-state transitions scales with the product of n_e and n_i,

$$\frac{dn_e}{dt} \approx n_e n_i \sum_Q \left(\alpha_Q^{\mathrm{CI}} - \alpha_Q^{\mathrm{DR}} - \alpha_Q^{\mathrm{RR}} - \alpha_Q^{\mathrm{3BR}}\right), \qquad (11)$$

so most ionization and recombination occurs in the dense target during the 2-ps runtime. Even if a hot plasma surrounds the target with a temperature high enough to strongly favor ionization, recombination will still dominate the system if the initial solid-density region is cool enough, as there are more particles present to undergo charge-state transition.

Using the electron temperature and number density from Fig. 7, combined with the number density of each ion species taken from the simulations, the approximate transition rate (11) can be used to estimate the number of real-particle transitions in each simulation cell. Figure 8 shows this expected transition count as a function of time over the initial target volume. In 100-nm targets, it can be seen that the $Au^{68+} \rightarrow Au^{69+}$ ionization rate is significantly higher than the recombination rates at all times, which explains the limited effect recombination has on the simulation. However, for 300-nm

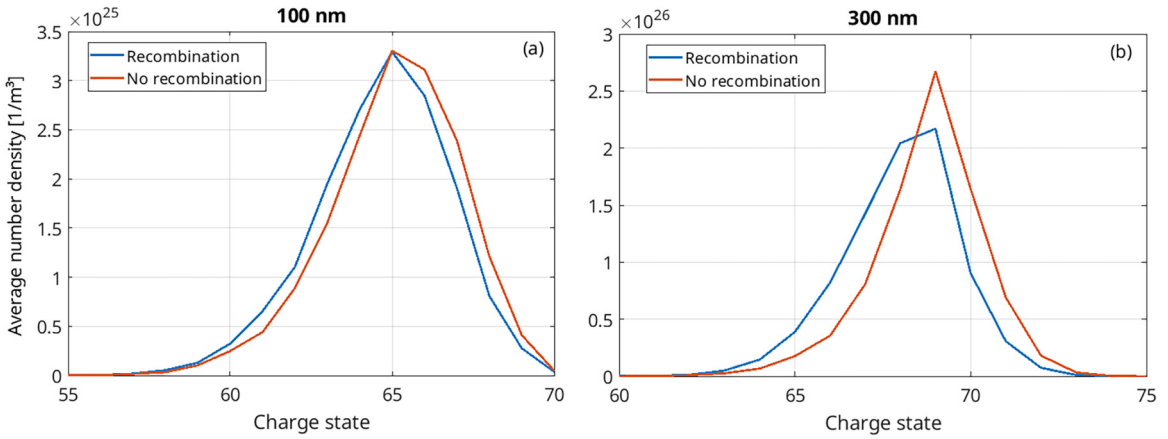

FIG. 6. Charge-state distribution snapshot at $t = 2$ ps from different simulations. Plot (a) shows distributions for the 100-nm target, with and without recombination, and (b) shows the same for 300-nm targets. The ion number densities have been averaged over a window from -9 μm to 9 μm.

targets, the temperature drops sufficiently low in the target volume that the combined recombination rates start to dominate CI, resulting in the charge-state drop seen in Figs. 5(d) and 6(b).

Figure 8 also shows the peak CI rate for Au^{68+} is significantly higher in the 300-nm case, which is due to the 100-nm target reaching lower charge-states overall, as in Fig. 6. It is clear from the electron density evolution plots in Fig. 7 that a greater electron density is sustained in the 300-nm targets, which implies more ionization is present overall. Lower temperatures in 300-nm targets could slow target expansion, maintaining a higher density of electrons for longer, which would in turn produce more ionization and obtain even higher electron densities for further ionization.

While it is instructive to consider the full evolution of the plasma, both the PHELIX experiment [1] and the original analysis [14] focused on the accelerated ion beams. Following the method of Afshari *et al.* [14], a probe was positioned at $x = 2$ μm, and the average flux of ions with kinetic energy over 1 MeV/u was recorded. These ion fluxes are shown in Fig. 9 and demonstrate similar trends to the full plasma behavior. The peak probe charge-state drops from around 61 to 60 when recombination is switched on for 100-nm targets, and from around 65 to 63 for 300 nm. Recombination has a smaller effect on the accelerated ions than on the full plasma shown in Fig. 6, where the entire distribution is shifted to lower charge-states instead of just the peak.

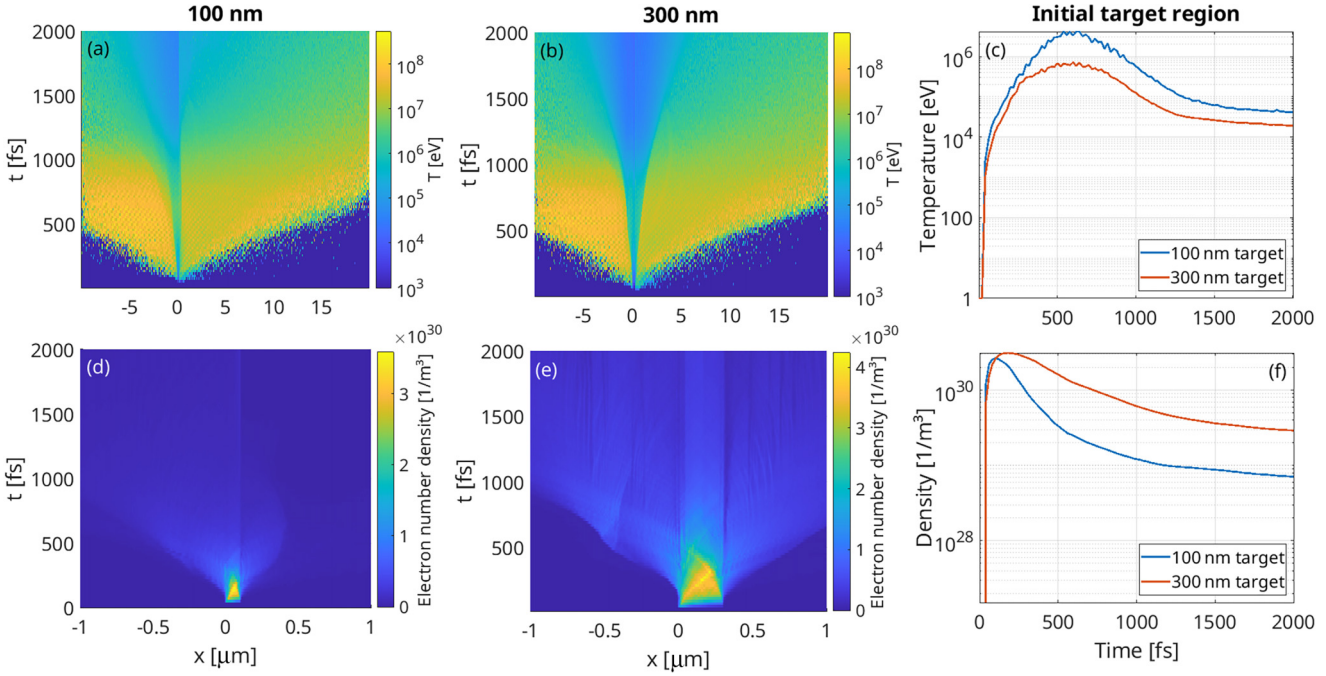

FIG. 7. Density and temperature evolution of simulations with recombination switched on. Plots (a) and (b) show the full temperature evolution for 100-nm and 300-nm targets, respectively, and (c) shows how the average temperature in the initial target volume changes with time. Plots (d), (e), and (f) match (a), (b), and (c), respectively, but show electron number density instead of temperature.

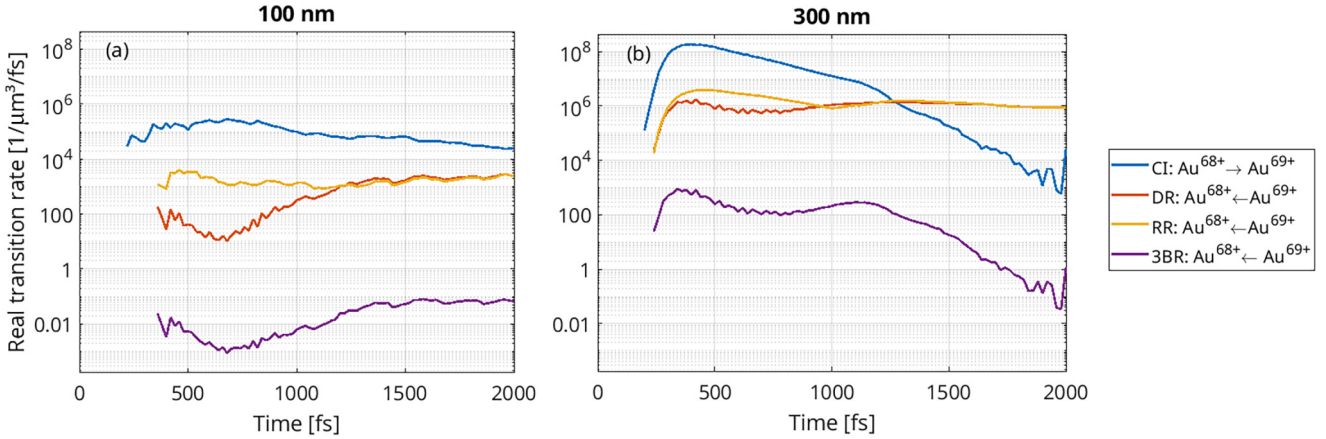

FIG. 8. Real transition rates between Au^{68+} and Au^{69+} ions in the initial target volume, for (a) 100-nm target and (b) 300-nm target. Rates are calculated using Eq. (11), such that the integral between two time points yields the total number of ions transitioning over that time interval per cubic micron. This calculation includes the local electron and ion number densities, and the temperature at each time.

The differing recombination changes shown in Figs. 6(b) and 9(b) can be explained by inspecting the times when ions pass the probe. Figure 10 shows the temporal evolution of energetic ion flux at the probe for each charge-state. Lower charge-states arrive at the probe earlier, with the highest charge-states arriving between 500 fs and 1 ps. At these times, ionization of the highest charge-states still dominates recombination within the target, as seen in Fig. 8(b). The later cooling responsible for the recombination dominance in Fig. 6(b) has not yet started by the time ions pass the probe in Fig. 9(b). Any differences in the probe particles are most likely due to recombination as the target is initially heated. Since the targets start cold, it will take longer to populate the higher charge-states when ionization is competing with recombination. Figure 7 shows the 100-nm target heats faster than the 300-nm target, which explains why the 100-nm target is less affected.

While it has been shown that recombination rates are sufficient to affect the charge-state distributions of the plasma and the ion beam, there are still discrepancies compared to experiment and 2D simulations. The PHELIX experiment observed higher charge-states than were achieved in Fig. 9, with the experiment finding dominant ion-beam charge-states of Au^{69+} and Au^{65+} for 100-nm and 300-nm targets, respectively [1]. 2D simulations could achieve these high charge-states but suggested that recombination should cause ion beams to drop 4–5 charge-states in 300-nm targets, instead of the two shown in Fig. 9 [14]. These observations are likely due to the limitations of 1D modeling. A 2D simulation would introduce a laser profile and could include self-focusing to produce more localized high-temperature regions where ionization dominates. The transverse drop-off in the laser profile would also keep parts of the target colder for longer, allowing more time for recombination, too. Although 1D modeling may lack a fully predictive capability, the reduced computational cost allows for high-resolution heat-flow modeling, which provides a greater insight into the role of recombination in these heavy-ion acceleration experiments.

V. CONCLUSION

A recombination package for PIC codes has been developed and applied to study the charge-state distributions expected in heavy-ion acceleration. It was found that thin

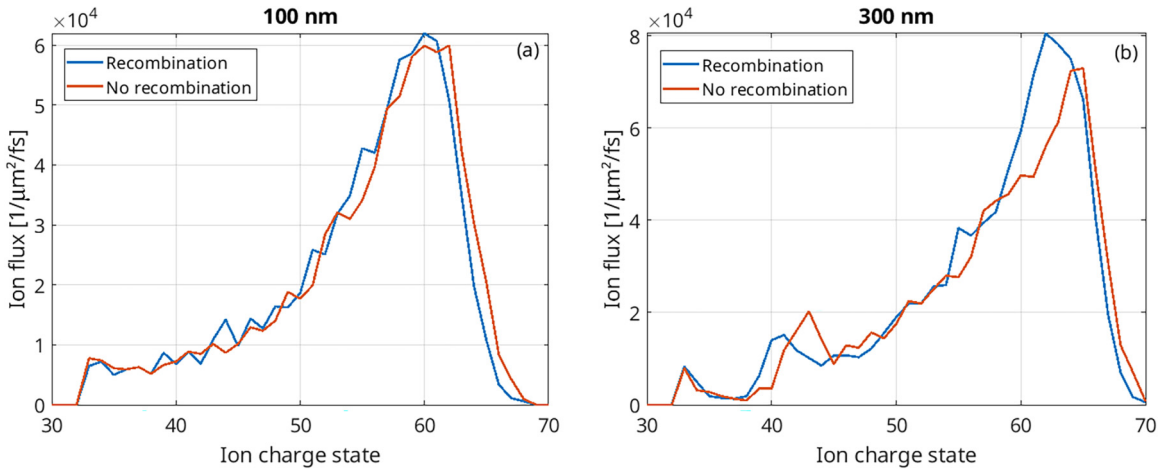

FIG. 9. Total flux of energetic ions (kinetic energy over 1 MeV/u) passing a particle probe positioned at $x = 2$ μm, averaged over a 2-ps window. The figure includes different simulations with 100-nm targets and 300-nm targets for (a) and (b), respectively.

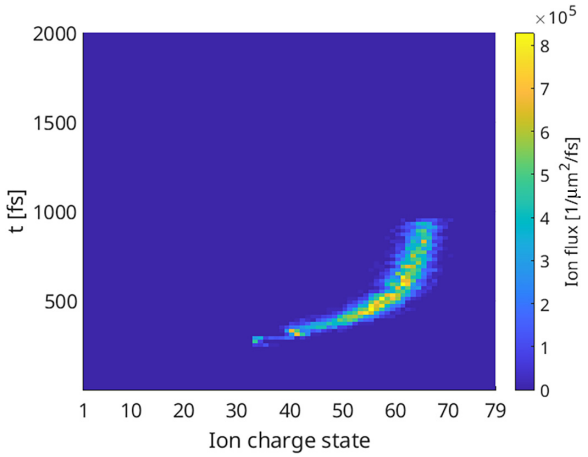

FIG. 10. Flux of energetic ions (kinetic energy over 1 MeV/u) passing the $x = 2$-μm particle probe as a function of time and charge state. Data is taken from the 300-nm target simulation with recombination switched on.

targets were mostly unaffected by recombination, due to the high temperatures achieved over a 2-ps window. Conversely, the lower temperatures reached in thicker targets allowed recombination effects to modify the final ion charge-states, although this was less pronounced in the ion beam itself. These simulated observations broadly agree with the experimental trends [1] and could explain why ion-beam charge-states decrease in thicker targets. While the 1D simulations were unable to fully reproduce experimental data [1] or match output from 2D simulations [14], these results do show that recombination can play a role in the acceleration of heavy ions.

ACKNOWLEDGMENTS

This work was supported by the UK Engineering and Physical Sciences Research Council (EPSRC) through Grant No. EP/W03008X/1. The EPOCH code used in this project was funded by UK EPSRC Grants No. EP/G054950/1, No. EP/G056803/1, No. EP/G055165/1, and No. EP/M022463/1. Computing facilities were provided by the Scientific Computing Research Technology Platform of the University of Warwick. This research was also funded in part by Fundação para a Ciência e Tecnologia (FCT, Portugal) through Research Center Grant No. UID/FIS/04559/2020 to LIBPhys-UNL from the FCT/MCTES/PIDDAC, Portugal. We acknowledge support from the Leibniz Supercomputing Centre (LRZ) under Application No. 24836. We are also grateful for the efforts of Tony Arber (University of Warwick) and Michael Bussmann (CASUS), who were both involved in grant applications which directly supported this work.

APPENDIX A: LORENTZ-BOOSTED TEMPERATURE

To obtain electron temperatures in EPOCH, the thermal energy $3k_BT_e/2$ is equated to the mean electron kinetic energy, yielding

$$T_e = \frac{\langle p^2 \rangle_e}{3m_e k_B} \tag{A1}$$

for momentum p, where $\langle ... \rangle_e$ describes an average over all electrons in the cell. The nonrelativistic form of kinetic energy is appropriate here, as recombination can be ignored at relativistic electron temperatures. However, for accelerated gold ions, the recombination rates are only valid for the temperature in the ion rest frame.

Assuming an isotropic distribution of electrons, let us arbitrarily choose a coordinate system where ion motion is in the x direction. The electron momenta in the ion rest frame (marked $'$) are given by

$$p'_x = \gamma_i \left(p_x - \beta_i \frac{E_e}{c} \right) \tag{A2}$$

$$p'_y = p_y \tag{A3}$$

$$p'_z = p_z, \tag{A4}$$

where γ_i and β_i are the relativistic Lorentz factor and ratio of velocity to c for the ion, respectively, and E_e is the total relativistic electron energy, with all terms evaluated in the simulation frame. From the isotropic simulation-frame assumption, $\langle p_x^2 \rangle = \langle p_y^2 \rangle = \langle p_z^2 \rangle = \langle p^2 \rangle / 3$. Hence, the electron temperature evaluated in the ion rest frame may be written

$$T'_e = \frac{\langle p'^2_x \rangle_e + \langle p'^2_y \rangle_e + \langle p'^2_z \rangle_e}{3m_e k_B}, \tag{A5}$$

$$T'_e = \frac{1}{3m_e k_B} \left[\left(\frac{1}{3}\gamma_i^2 + \frac{2}{3} + \gamma_i^2 \beta_i^2 \right) \langle p^2 \rangle_e + (\gamma_i \beta_i m_e c)^2 - \frac{2\beta_i \gamma_i^2}{c} \langle p_x E_e \rangle_e \right]. \tag{A6}$$

Therefore, EPOCH may evaluate the electron temperature in any ion rest frame by precalculating the values of $\langle p^2 \rangle_e$ and $\langle p_x E_e \rangle_e$ in the simulation frame first. The code does not need to transform each electron to the ion rest frame individually for each ion present, as that would be a prohibitively slow operation.

APPENDIX B: RECOMBINATION SAMPLING EXAMPLES

This Appendix provides two examples to show how the recombination sampling algorithm works for arbitrarily weighted macroparticles. In the first case, consider a cell with 100 macroelectrons and 200 macroions of weight $W_i = 5$, representing 1000 real ions. Let each macroelectron have weight $W_e = 10$, and $N_r = 2$ from Eq. (8), such that there are 1000 real electrons and each has a 20% chance of recombining over Δt. The algorithm should therefore act to recombine 200 real electrons with 200 real ions. Following the procedure of Sec. III A, all 100 macroelectrons are randomly paired with 100 of the 200 macroions. Since $W_i > N_r$ in all pairs, macroions only recombine with probability $N_r/W_i = 0.4$. This causes 40 macroions of weight 5 to recombine on average, or 200 real ions as expected. Each macroelectron is removed with probability N_r/W_e, so roughly 20 macroelectrons of weight 10 are removed, again achieving the expected 200 real electrons recombining on average.

For the second case, consider a cell with $W_i < N_r$. Suppose one macroelectron with $W_e = 100$, $N_r = 25$ sits in a cell with

ten macroions of weight $W_i = 10$. In the first electron-ion pairing, $W_i < N_r$, so the macroion is tagged to recombine. Following Eq. (10), $f_e \to 0.6$, and a new partner is found for the macroelectron, with $N_r = 25$, and $f_e N_r = 15$. We still have $f_e N_r > W_i$, so the new macroion is also tagged to recombine and $f_e \to 0.2$. Now $f_e N_r = 5$, so the next electron-ion pairing only recombines the macroion with probability $f_e N_r / W_i = 0.5$. This macroelectron will therefore trigger 2.5 macroions to recombine on average, achieving the expected 25 real ions. The macroelectron is removed with probability $N_r / W_e = 0.25$.

A macroion which fails the recombination test can be resampled by other macroelectrons, and the sampling will end if there are no more macroions left in the cell to recombine. When a macroelectron is paired to a new macroion in the code, a new N_r is calculated using the new relative momentum of the electron-ion pair, but N_r has been assumed constant in this Appendix.

[1] F. H. Lindner, E. Fitzpatrick, D. Haffa, L. Ponnath, A.-K. Schmidt, M. Speicher, B. Zielbauer, J. Schreiber, and P. Thirolf, Charge-state resolved laser acceleration of gold ions to beyond 7 meV/u, Sci. Rep. **12**, 4784 (2022).

[2] P. Martin, H. Ahmed, D. Doria, M. Cerchez, F. Hanton, D. Gwynne, A. Alejo, J. Fernández-Tobías, J. Green, A. Macchi *et al.*, Narrow-band acceleration of gold ions to GeV energies from ultra-thin foils, Commun. Phys. **7**, 3 (2024).

[3] P. Wang, Z. Gong, S. G. Lee, Y. Shou, Y. Geng, C. Jeon, I. J. Kim, H. W. Lee, J. W. Yoon, J. H. Sung *et al.*, Super-heavy ions acceleration driven by ultrashort laser pulses at ultrahigh intensity, Phys. Rev. X **11**, 021049 (2021).

[4] J. Braenzel, A. A. Andreev, K. Platonov, M. Klingsporn, L. Ehrentraut, W. Sandner, and M. Schnürer, Coulomb-driven energy boost of heavy ions for laser-plasma acceleration, Phys. Rev. Lett. **114**, 124801 (2015).

[5] D. Habs, P. Thirolf, M. Gross, K. Allinger, J. Bin, A. Henig, D. Kiefer, W. Ma, and J. Schreiber, Introducing the fission–fusion reaction process: using a laser-accelerated Th beam to produce neutron-rich nuclei towards the $N = 126$ waiting point of the *r*-process, Appl. Phys. B **103**, 471 (2011).

[6] M. Arnould, S. Goriely, and K. Takahashi, The r-process of stellar nucleosynthesis: Astrophysics and nuclear physics achievements and mysteries, Phys. Rep. **450**, 97 (2007).

[7] T. G. White, J. Vorberger, C. Brown, B. Crowley, P. Davis, S. Glenzer, J. Harris, D. Hochhaus, S. Le Pape, T. Ma *et al.*, Observation of inhibited electron-ion coupling in strongly heated graphite, Sci. Rep. **2**, 889 (2012).

[8] A. Pelka, G. Gregori, D. O. Gericke, J. Vorberger, S. H. Glenzer, M. M. Günther, K. Harres, R. Heathcote, A. L. Kritcher, N. L. Kugland, B. Li, M. Makita, J. Mithen, D. Neely, C. Niemann, A. Otten, D. Riley, G. Schaumann, M. Schollmeier, A. Tauschwitz, and M. Roth, Ultrafast melting of carbon induced by intense proton beams, Phys. Rev. Lett. **105**, 265701 (2010).

[9] W. Bang, B. Albright, P. Bradley, D. Gautier, S. Palaniyappan, E. Vold, M. S. Cordoba, C. Hamilton, and J. Fernández, Visualization of expanding warm dense gold and diamond heated rapidly by laser-generated ion beams, Sci. Rep. **5**, 14318 (2015).

[10] S. Kawata, T. Karino, and A. Ogoyski, Review of heavy-ion inertial fusion physics, Matter Radiat. Extremes **1**, 89 (2016).

[11] M. Roth, T. E. Cowan, M. H. Key, S. P. Hatchett, C. Brown, W. Fountain, J. Johnson, D. M. Pennington, R. A. Snavely, S. C. Wilks, K. Yasuike, H. Ruhl, P. Pegoraro, S. V. Bulanov, E. M. Campbell, M. D. Perry, and H. Powell, Fast ignition by intense laser-accelerated proton beams, Phys. Rev. Lett. **86**, 436 (2001).

[12] D. Schardt, T. Elsässer, and D. Schulz-Ertner, Heavy-ion tumor therapy: Physical and radiobiological benefits, Rev. Mod. Phys. **82**, 383 (2010).

[13] O. Jäkel, G. Kraft, and C. P. Karger, The history of ion beam therapy in germany, Z. Med. Phys. **32**, 6 (2022).

[14] M. Afshari, S. Morris, L. Geulig, Z. Chitgar, P. Gibbon, P. Thirolf, and J. Schreiber, The role of collisional ionization in heavy ion acceleration by high intensity laser pulses, Sci. Rep. **12**, 18260 (2022).

[15] G. Petrov, C. McGuffey, A. Thomas, K. Krushelnick, and F. Beg, Generation of heavy ion beams using femtosecond laser pulses in the target normal sheath acceleration and radiation pressure acceleration regimes, Phys. Plasmas **23**, 063108 (2016).

[16] J. Domański and J. Badziak, Super-heavy ion beams generated by a multi-PW femtosecond laser, Phys. Plasmas **31**, 023110 (2024).

[17] T. Arber, K. Bennett, C. Brady, A. Lawrence-Douglas, M. Ramsay, N. Sircombe, P. Gillies, R. Evans, H. Schmitz, A. Bell *et al.*, Contemporary particle-in-cell approach to laser-plasma modelling, Plasma Phys. Control. Fusion **57**, 113001 (2015).

[18] L. Keldysh *et al.*, Ionization in the field of a strong electromagnetic wave, in *Selected Papers of Leonid V Keldysh* (World Scientific, 2023), pp. 56–63.

[19] S. Morris, T. Goffrey, K. Bennett, and T. Arber, Improvements to collisional ionization models for particle-in-cell codes, Phys. Plasmas **29**, 123907 (2022).

[20] D. Wu, X. T. He, W. Yu, and S. Fritzsche, Monte Carlo approach to calculate ionization dynamics of hot solid-density plasmas within particle-in-cell simulations, Phys. Rev. E **95**, 023208 (2017).

[21] E. Khalilzadeh, J. Yazdanpanah, J. Jahanpanah, and A. Chakhmachi, Numerical modeling of radiative recombination during ionization of atoms by means of particle-in-cell simulation, Laser Part. Beams **34**, 284 (2016).

[22] J. Dubau and S. Volonte, Dielectronic recombination and its applications in astronomy, Rep. Prog. Phys. **43**, 199 (1980).

[23] H. A. Kramers, XCIII. On the theory of x-ray absorption and of the continuous x-ray spectrum, London, Edinburgh, Dublin Philos. Mag. J. Sci. **46**, 836 (1923).

[24] D. Kremp, M. Schlanges, and W.-D. Kraeft, *Quantum Statistics of Nonideal Plasmas* (Springer Science & Business Media, New York, 2005), Vol. 25.

[25] A. Lawrence-Douglas, Ionisation effects for laser-plasma interactions by particle-in-cell code, Ph.D. thesis, University of Warwick, 2013.

[26] N. B. Delone and V. P. Kraĭnov, *Multiphoton Processes in Atoms* (Springer Science & Business Media, New York, 2000), Vol. 13.

[27] M. V. Ammosov, N. B. Delone, and V. P. Krainov, Tunnel ionization of complex atoms and of atomic ions in an

alternating electromagnetic field, Sov. J. Exp. Theor. Phys. **64**, 1191 (1986).

[28] J. Posthumus, The dynamics of small molecules in intense laser fields, Rep. Prog. Phys. **67**, 623 (2004).

[29] Y.-K. Kim, J. P. Santos, and F. Parente, Extension of the binary-encounter-dipole model to relativistic incident electrons, Phys. Rev. A **62**, 052710 (2000).

[30] J. P. Desclaux, A multiconfiguration relativistic Dirac-Fock program, Comput. Phys. Commun. **9**, 31 (1975).

[31] P. Indelicato and J. P. Desclaux, Multiconfiguration Dirac-Fock calculations of transition energies with QED corrections in three-electron ions, Phys. Rev. A **42**, 5139 (1990).

[32] G. Audi, A. H. Wapstra, and C. Thibault, The AME2003 atomic mass evaluation: (II) Tables, graphs and references, Nucl. Phys. A **729**, 337 (2003).

[33] I. Angeli, A consistent set of nuclear rms charge radii: properties of the radius surface $R(N,Z)$, At. Data Nucl. Data Tables **87**, 185 (2004).

[34] G. C. Rodrigues, P. Indelicato, J. P. Santos, P. Patté, and F. Parente, Systematic calculation of total atomic energies of ground state configurations, At. Data Nucl. Data Tables **86**, 117 (2004).

[35] H.-K. Chung, M. Chen, W. Morgan, Y. Ralchenko, and R. Lee, FLYCHK: Generalized population kinetics and spectral model for rapid spectroscopic analysis for all elements, High Energy Density Phys. **1**, 3 (2005).

[36] S. Fritzsche, Dielectronic recombination strengths and plasma rate coefficients of multiply charged ions, Astron. Astrophys. **656**, A163 (2021).

[37] S. Fritzsche, A fresh computational approach to atomic structures, processes and cascades, Comput. Phys. Commun. **240**, 1 (2019).

[38] S. Fritzsche, P. Palmeri, and S. Schippers, Atomic cascade computations, Symmetry **13**, 520 (2021).

[39] K. Nanbu and S. Yonemura, Weighted particles in Coulomb collision simulations based on the theory of a cumulative scattering angle, J. Comput. Phys. **145**, 639 (1998).

[40] F. Pérez, L. Gremillet, A. Decoster, M. Drouin, and E. Lefebvre, Improved modeling of relativistic collisions and collisional ionization in particle-in-cell codes, Phys. Plasmas **19**, 083104 (2012).